$BiVO_3$: A Bi-based material with promising uv-visible light absorption properties

C. S. Praveen*
Department of Chemistry and Applied Biosciences, ETH Zurich, Vladimir Prelog Weg 1-5, 8093 Zurich, Switzerland and Materials Research Laboratory, University of Nova Gorica, Vipavska 11c, 5270 Ajdovscina, Slovenia

Lorenzo Maschio†
Dipartimento di Chimica IFM, Università di Torino and NIS, Nanostructured Interfaces and Surfaces, Centre of Excellence, Via P. Giuria 7, 10125 Torino, Italy

Michel Rérat
Equipe de Chimie Physique, IPREM UMR5254, Université de Pau et des Pays de l'Adour, 64000 Pau, France

V. Timon
Instituto de Estructura de la Materia (CSIC), C/Serrano 113, 28006 Madrid, Spain

M. Valant
Materials Research Laboratory, University of Nova Gorica, Vipavska 11c, 5270 Ajdovscina, Slovenia and Institute of Fundamental and Frontier Sciences, University of Electronic Science and Technology of China, Chengdu 610054, China

(Received 5 June 2017; revised manuscript received 12 October 2017; published 30 October 2017)

Spin polarized density functional theory calculations on a predicted $BiVO_3$ crystal structure is presented. An orthorhombic phase with space group *Pnma* is observed to be highly stable compared to the aristotype cubic structure. An optical band gap of 1.92 eV and a strong optical absorption at 2.25 eV—which lie in the visible region of the solar spectra—are estimated at the coupled-perturbed hybrid density-functional theory level. In addition, the band-structure analysis somewhat shows dispersion at the valence and conduction bands, and the binding energy of the excitons is calculated to be quite low, which can be possibly dissociated at room temperature. $BiVO_3$ is, therefore, expected to be a promising candidate worth being investigated for visible light driven photocatalytic applications. Simulated infrared and Raman spectra are reported, which could represent a guideline for future experiments, along with a full characterization of structural, electronic, and dynamic properties.

DOI: 10.1103/PhysRevB.96.165152

I. INTRODUCTION

Efficient conversion and utilization of solar energy [1–4] to meet the planetary needs for addressing future energy demands have gained profound attention at a global level [5–8]. Water and air purification and hydrogen fuel production by the splitting of water using solar energy have a terrestrial demand and urgency. Since hydrogen is considered as "the fuel of the future," its cost effective production by solar water splitting has gained a particular focus [5,9,10].

To date, no single candidate has met all the requirements for photocatalytic water splitting under visible light, with an economically viable efficiency (approximately 10%) [5,9–14] to provide a route to human's dreams on a hydrogen fuel based future. In addition to the countless efforts in improving the catalytic activity of existing photocatalytic semiconductors, such as TiO_2 [15], Fe_2O_3 [16], $BiVO_4$ [17,18], much attention has been paid to developing single phase metal oxide visible-light active photocatalysts. However, the challenge is still open as metal oxides are poor visible light absorbers (band gap >3 eV), despite their excellent chemical stability.

It has been demonstrated [19,20] that the 6*s* orbitals in Pb^{2+} and Bi^{3+}, 5*s* orbitals in Sn^{2+}, and 4*d* orbitals in Ag^{4+} can form valence levels above the O-2*p* valence levels. The contribution of these orbitals to the valence band depends on the crystal structure and the concentration of the metal cations in the compound. Thus, an oxide semiconductor with a narrow band gap can be developed by incorporating the aforementioned cations in the structure. From a structural point of view, generic ABO_3 perovskites are good starting structures, as their compositional and structural flexibility enables a variety of fascinating properties such as ferroelectricity, superconductivity, ferromagnetism, antiferromagnetism, and large dielectric constants. Several perovskites have shown stable photocatalytic activity under illumination, e.g., $SrTiO_3$ [21], $NaTaO_3$ [22], $KTaO_3$ [22], $AgTaO_3$ [23]. Many Bi-based (especially with transition metals) low band-gap semiconductors have also been realized, e.g., $BiVO_4$ (2.4 eV) [24], $BiInO_3$ (2.08 eV) [25], $BiGaO_3$ (2.03 eV) [26], $BiCrO_3$ (1.5 eV) [27], $BiMnO_3$ (1.1 eV) [28], $BiFeO_3$ (2.5 eV) [29].

In addition to the observed catalytic activity, Bi-based (Bi^{3+}) oxide perovskites have recently gained much interest due to their multifunctionality [30,31]. Bi-based transition-metal oxides can be considered as an alternative to lead-free ferroelectric and multiferroic materials [32–35]. The $6s^2$ lone pair electrons in Bi/Pb, in general, have a tendency to off-center the respective ions from their ideal positions in the polyhedral. This off-centring could lead to ferroelectricity [33,35,36]. In addition to the off-centring driven ferroelectricity, for the material to be multiferroic, a partially filled

*Corresponding author: praveen.chandramathy@mat.ethz.ch
†http://www.nis.unito.it

transition-metal ion should be present at the B site to drive ferro-antiferromagnetism.

Hence, incorporation of transition metals at the B site in Bi-based perovskites has been intensively investigated for the past few years. Among the first row transition metals, Bi-based perovskites with Sc, Cr, Fe, Mn, Co, and Ni at the B site have already been realized. Among them, $BiFeO_3$ and $BiMnO_3$ have been extensively investigated and they are demonstrated to be multiferroic [27,32,37]. Early attempts to synthesize $BiVO_3$ [38,39] and $BiTiO_3$ [38] have not been successful due to the oxidation of V^{3+} and Ti^{3+} to their 4+ oxidation state, which resulted in the formation of $Bi_4M_3O_{12}$ (M = V,Ti) [38,40]. No attempts to synthesize $BiCuO_3$ have yet been reported. Because of this, almost nothing is known about either the stability or the properties of the V^{3+}, Ti^{3+}, and Cu^{3+} perovskites. A $BiVO_3$ structure has been preliminarily reported in thin perovskite films [41]. Recently Liu *et al.* have reported a computational work on bulk $BiVO_3$ in its antiferromagnetic state [42].

In this work, we start from the structure predicted by the SPUDS software [43], and present a complete *ab initio* characterization of the structural, electronic, magnetic, and dynamical properties of the paraelectric phase of $BiVO_3$.

II. COMPUTATIONAL DETAILS

All the density-functional theory calculations presented here were performed using a development version of the CRYSTAL code [44]. Two functionals have been adopted throughout, a B1WC hybrid functional, as well as PBE16, a Perdew-Burke-Ernzerhof (PBE) functional for the exchange and correlation together with 16% Hartree-Fock exchange, which is expected to be suitable for the description of dielectric and optical properties where the value 16% was obtained as the inverse of the dielectric constant $1/(\varepsilon_\infty)$ [45]. Other details as well as computational settings regarding basis set choice and other thresholds can be found in the Supplementary Information [46]. IR, Raman, and optical-absorption spectra have been computed analytically, thanks to the corresponding modules in CRYSTAL, based on coupled-perturbed Hartree-Fock/Kohn-Sham (CPHF/KS) treatments [47–50].

III. RESULTS AND DISCUSSION

A. Structural properties

The *Pnma* structure can be thought of as being formed by repeated tilting of the VO_6 octahedral unit in a zigzag manner ($GdFeO_3$-type distortion [51]) as shown in Fig. 1. The tilting can be assigned as two antiphase tilts of equal magnitude (i.e., $a^-b^+a^-$) with respect to the [100] and [001] pseudocubic axes and an in-phase tilt with respect to the [010] pseudocubic axes. The tilting results in a decrease in symmetry

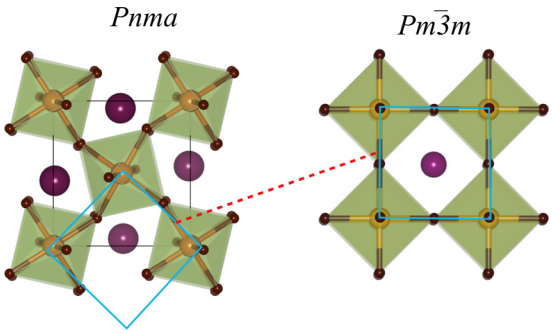

FIG. 1. *Pnma* structure (left) is shown as a distorted derivative of the cubic structure (right). For a clear indication of the nature of the distortion, the undistorted cubic part is notated as a blue square. Coloring of the atoms is as follows: Bi (dark magenta); V (dark orange (left); O (dark brown).

as well as in an increase in the size of the unit cell from one formula unit (five atoms) for the cubic cell to four formula units (20 atoms) for the orthorhombic cell. The total energy of the aristotype cubic and the hettotype orthorhombic structures after relaxing the geometry are presented in Table I. As seen from the table, the ferromagnetic orthorhombic structure is 1.275 eV/f.u. lower in energy compared to the cubic structure. Thus, structurally the orthorhombic phase is far more stable than the cubic. In addition, the B1WC functional predicts the electronic nature of the cubic structure as conducting while that of the orthorhombic structure as semiconducting. This further corroborates that the cubic structure is less likely to be the ground state of $BiVO_3$ crystal. Similar instabilities for the cubic structures are noticed for the other perovskites from the same family: for example, Ravindran *et al.* [30] have shown the instability of the cubic phase of $BiFeO_3$ because of its higher energy (1.1 eV/f.u) compared to the $R3c$ phase. Since the cubic structure is shown to be less stable, from here onward we focus mainly on the hettotype orthorhombic *Pnma* structure, and data from the cubic structure will be provided when a comparison is indispensable. The *Pnma* structure has a point-group symmetry of D_{2h}, with four formula units per unit cell. Therefore, there are four transition metal atoms in the unit cell and this allows assigning different antiferromagnetic structures in addition to the ferromagnetic structure.

In our case we have assigned all the possible three antiferromagnetic orderings, namely A type (A AFM), G type (G AFM), and C type (C AFM). The total energies of all three relaxed antiferromagnetic structures are collected in Table I. As it can be seen from the table, the energy difference between the ferromagnetic and the antiferromagnetic structures is very small. These nearly degenerate energies indicate a high level of competition among the FM and the AFM states and possibility

TABLE I. Total energy per formula unit (f.u.) of cubic ($Pm\bar{3}m$) and orthorhombic ($Pnma$) $BiVO_3$. The energy of the ferromagnetic *Pnma* structure is taken as the reference energy. Total energy corresponds to different antiferromagnetic settings of *Pnma*; A AFM, C AFM, and G AFM is also provided.

Structure	($Pm\bar{3}m$) (FM)	*Pnma* (FM)	*Pnma* (A AFM)	*Pnma* (G AFM)	*Pnma* (C AFM)
TE (eV/f.u.)	−31 955.68	−31 956.95	−31 956.93	−31 956.91	−31 956.93
$\Delta E = \left(E - E^{FM}_{Pnma}\right)$ (eV)	1.275	0.0	0.02475	0.0466	0.0277

TABLE II. Population analysis: the nearest-neighbor cation-anion distance, bond populations, and cation-anion bridging angle. Values in the parentheses show the corresponding parameters in the cubic structure.

Cation-anion pair *Pnma*	Distance (Å)	Bond population
Bi-O1	2.28	−0.064
Bi-O2	2.39	−0.089
Bi-O3	2.00	0.039
V1-O1	2.02	0.034
V1-O2	2.03	0.037
V1-O3	1.99	0.038
V2-O1	2.04	0.027
V2-O2	2.01	0.040
V3-O3	2.26	−0.069
V-O-V	bond angle (deg)	
V1-O1-V2	148.8° (180°)	
V1-O2-V2	149.6°	
V1-O3-V2	147.3°	

on a magnetic phase transition even at low temperature. In the present study, the slightly more stable FM (approximately 25 meV compared to the close lying AFM state) state is considered as the ground state of $BiVO_3$, on which a full characterization of the structural electronic and vibrational properties is performed.

The calculation showed that the perovskite $BiVO_3$ ground-state structure is orthorhombic *Pnma* (D_{2h}). The assigned Wyckoff positions as well as the optimized atomic coordinates are reported in the Supplemental Material [46]. The lattice parameters calculated for the *Pnma* structure from the cubic structure are given in Table II in parentheses. The table shows that the lattice parameters are in good agreement with the values predicted from the cubic lattice parameter. The optimized structure of orthorhombic $BiVO_3$ is shown in Fig. 2 and the corresponding bond lengths are presented in the Supplemental Material [46].

B. Electronic properties

In Fig. 3, we have plotted the band structure of $BiVO_3$, both in the up spin and down spin channel along eight high-symmetry points in the irreducible part of the Brillouin zone (BZ).

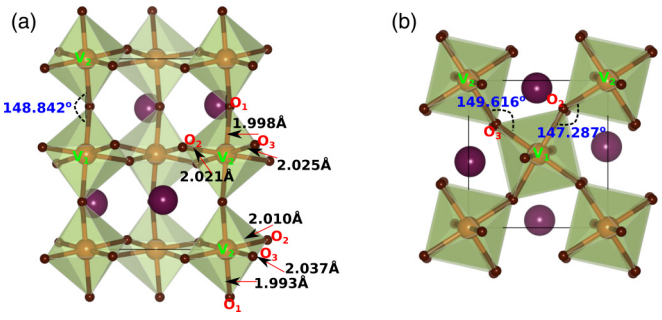

FIG. 2. Optimized structure of FM-$BiVO_3$. The bond lengths are measured in Å and the angles are measured in degrees. (a) Projection along the *c* axis; (b) projection along the *b* axis. Coloring of the atoms is same as in Fig. 1.

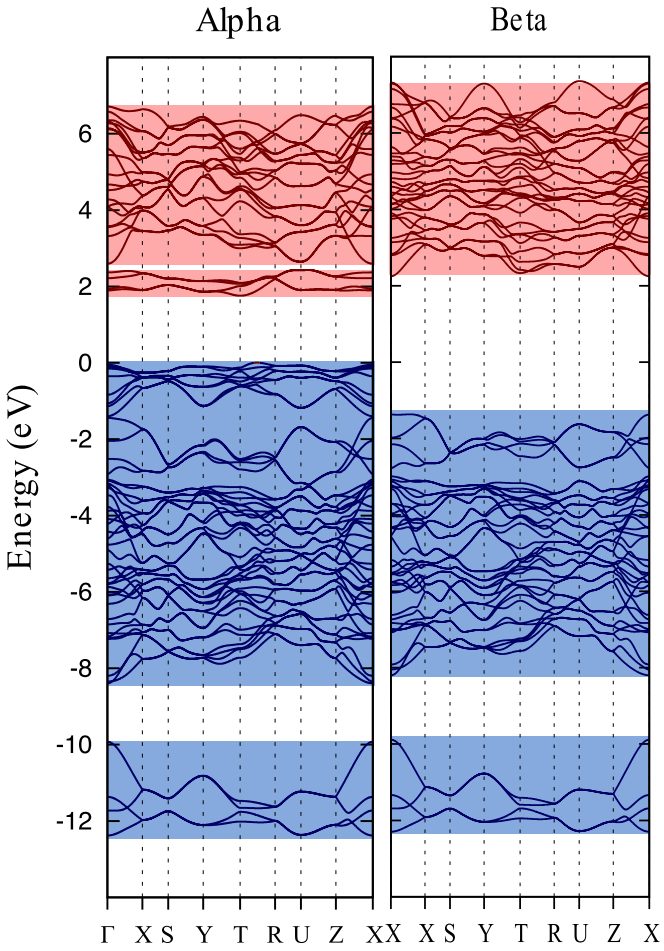

FIG. 3. Band structure (alpha and beta) of the paraelectric ferromagnetic phase of $BiVO_3$ plotted along the high-symmetric points in the irreducible part of the first Brillouin zone. The shapes of the Brillouin zone as well as the special points in the BZ are notated at the right panel.

The calculated indirect band gap is 1.76 eV. A direct band-gap value of 1.96 eV is calculated at the Γ point (center of the BZ) and this value indeed falls in the visible region of the spectra. Such a calculated low band-gap value is in line with the general trend from the Bi-based transition metal perovskite family, e.g., $BiCrO_3$ (1.5 eV) [27], $BiMnO_3$ (1.1 eV) [28], $BiFeO_3$ (2.5 eV) [29].

Further analysis of the bands shows that the bands are reasonably well dispersed throughout the valence- and conduction-band range, despite the relatively flatter bands at the band edges. Apparently, the comparatively higher dispersion in the bands is an indication of lesser effective mass for the charge carriers (holes in the valence band and electrons in the conduction band). As a direct consequence, holes and electrons could expect to have higher mobility in the respective bands, enhancing charge-carrier kinetics. This one-to-one correspondence between the dispersion in the band structure and the high mobility of the charge carriers has been demonstrated in many photocatalytic materials; for instance see Kudo *et al.* [24] and Kim *et al.* [52]. For a more quantitative assessment see below.

To gain a qualitative insight into the nature of the bands, the reader can find in Supplemental Material plots for the total

TABLE III. Static (ε_0) and optical dielectric (ε_∞) constants of $BiVO_3$ in different Cartesian directions.

Component	ε_0	ε_∞
xx	48.62	6.91
yy	96.74	6.97
zz	39.90	6.75
$zx = yz$	−1.13	−0.10

and atom projected density of states [46]. It is seen that in the lower edge of the upper valence band, the O-2p orbitals are dominant, while the energy range closer to the top of the valence band is dominated by the vanadium 3d levels, while the lower conduction band is predominantly contributed by the V-3d orbitals.

C. Dielectric properties

1. Static and optical dielectric constants

As already mentioned, for a better description of dielectric properties a PBE16 functional was adopted following the "inverse dielectric constant" proposal for weighting the exchange [45]. The calculated optical (ε_∞) and static (ε_0) dielectric constants are given in Table III. The vibrational contribution to the static dielectric constant is computed from the phonon spectrum using Eq. (1):

$$\epsilon_0 = \epsilon_\infty + \epsilon_{vib} = \epsilon_\infty + \frac{4\pi}{V}\sum_p \frac{Z_p^2}{\nu_p^2}, \tag{1}$$

where ν_p and Z_p are the phonon frequency of the mode p and the mass-weighted mode effective Born vector respectively, while V is the volume of the unit cell. The static dielectric tensor is highly isotropic for orthorhombic crystals. The rather high value of the optical dielectric constant (electronic contribution) reflects the extremely high polarizability of the crystal. On the other hand, the static dielectric constant (ε_0) (sum of electronic and vibrational contributions) shows the ionic degree of freedom. Unlike (ε_∞), the (ε_0) is highly anisotropic along different Cartesian directions. The high values of the dielectric constant are to be ascribed to strong covalent bonding between V-O and to the anomalous Born effective charges as we shall see below.

2. Born effective charge tensor

The Born charge tensor (Z^*) is a fundamental quantity in describing the lattice dynamics of a complex crystal. It is formally obtained as a mixed derivative of total energy with respect to both external electric field and atomic displacements [47], and is related both to infrared absorption intensities and LO-TO splitting in three-dimensional (3D) crystals.

The calculated Born effective charge tensor is given in Table IV. The formal valence charge of Bi, V, and O in $BiVO_3$ are +3, +3, and −2 respectively. Due to the ferromagnetic nature of the crystal, the site symmetry is reduced from D_{2h} to C_{2h} as discussed in the previous section. As a consequence of this, a large anisotropy is observed in the diagonal values of the Z^* tensor as evidenced from Table IV.

TABLE IV. Born effective charge tensor of $BiVO_3$ in different Cartesian directions.

Atom	Z^*_{XX}	Z^*_{YY}	Z^*_{ZZ}	Z^*_{xy}	Z^*_{xz}	Z^*_{yx}	Z^*_{yz}	Z^*_{zx}	Z^*_{zy}
Bi (4f)	4.90	5.07	4.96	0.21	0.11	0.12	−0.18	0.52	−0.13
V1 (2d)	4.26	3.95	3.25	−0.50	0.03	−0.22	0.03	−0.27	−0.35
V2 (2a)	3.79	4.00	3.78	0.15	−1.11	0.34	−0.06	−0.75	0.27
O1 (4f)	−2.42	−3.42	−2.85	−0.14	−0.65	0.24	0.26	−0.59	0.11
O2 (4f)	−3.00	−2.88	−2.58	−0.31	−0.17	−0.20	−0.17	−0.11	−0.21
O3 (4f)	−3.00	−2.88	−2.58	0.31	0.17	0.20	−0.17	0.11	−0.21

A high value for the Born charge tensor is an indication of the off-centring tendency of an atom by covalent bond formation (often considered as an indication of ferroelectricity), hence it triggers a much higher spontaneous polarization when a relative displacement of adjacent atoms occurs. As shown in Table IV, the Z^* value of Bi is very high ($Z^*_{zz} = 4.96$) compared to its nominal value (+3); this indicates the strong tendency of Bi atoms to off-center due to the lone pair effect. Similar high values of Z^* for the Bi ion are reported for many other Bi-based perovskite oxides [e.g., $BiFeO_3$ ($Z^*_{Bi} = 4.23$)] [40]. In order to build up the spontaneous polarization, the centrosymmetry has to be lifted. However, in the present case the FM structure of $BiVO_3$ remains centrosymmetric and thus shows zero spontaneous polarization, i.e., the crystal remains paraelectric.

The Z^* value for Bi shows a variation of +1.9 to +2.1 from its ideal ionic value. This shows a charge transfer between the np orbitals of the nearest-neighboring Bi and O atoms. As discussed earlier, this is a direct consequence of the lone pair effect and can be linked to the small Mulliken charge of −1.14 $|e|$ on the O atom (see Table I in the Supplemental Material [46]). Conversely, the noticeable off-diagonal components in all the three oxygen sites is a clear indication of a large hybridization between the V-3d orbitals and the O-2p orbitals and this is consistent with the Mulliken population analysis.

3. Binding energy of the exciton

The binding energy of the exciton is calculated using the Mott-Wannier exciton model [53], wherein the delocalized exciton is treated as a hydrogen atom, the hole being the proton. Within this approximation, the binding energy is calculated as

$$E_b = E_H \frac{\mu}{\varepsilon_r^2}, \tag{2}$$

where E_H is the energy of the 1s orbital of hydrogen (−13.6 eV) and μ is the reduced mass of the exciton. Since the method is used only as a rough estimation of the order of the binding energy, we calculated the reduced mass as follows:

$$\frac{1}{\mu} = \frac{1}{m_e^*} + \frac{1}{m_h^*}. \tag{3}$$

Here, the effective mass of the electrons m_e^* and holes m_h^* is calculated by fitting the bottom of the conduction band and top of the valence band, respectively to parabolic functions. The smallest value for the inverse of the reduced mass obtained is 2.55, along the (110)-(011) direction (S-T) in the electronic band structure. For photovoltaic and photochemical devices, it can be assumed that the time scale of the exciton dissociation

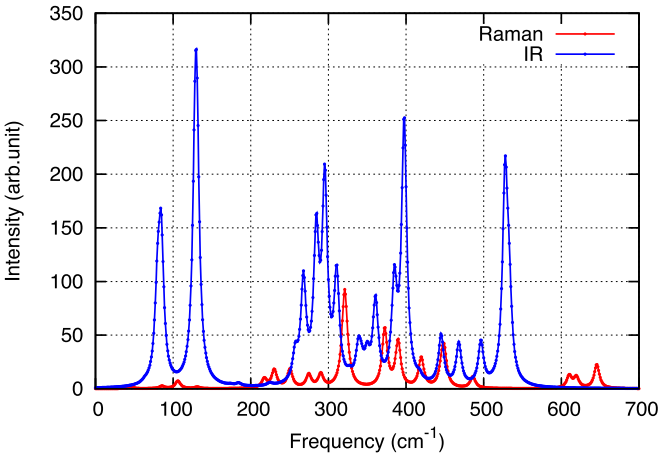

FIG. 4. IR and Raman absorption spectra.

is higher than the atomic motions. Therefore, it is assumed that the charge screening is governed by the relaxed exciton [54], then the relative dielectric ε_r in the binding energy expression given in Eq. (2) is given by the static dielectric matrix ε_0 (the components of which are reported in Table III). The ε_0 is calculated from the diagonal elements as 72.7 along (110) and 68.3 along (011). The geometrical mean of ε_0 along (110) and (011), i.e., 70.0 has been used for the evaluation of the binding energy. The calculated relaxed binding energy $E_b = -7$ meV is much lower (absolute value) than 25 meV (room temperature) and therefore the excitons could be easily dissociated at room temperature. On the other hand, if only the unrelaxed exciton is considered, the unrelaxed binding energy can be calculated by considering the average value of the optical dielectric const (ε_∞). The unrelaxed binding energy thus calculated is 700 meV, which is two orders of magnitude higher than the relaxed binding energy.

D. Optical properties

1. Infrared and Raman spectra

The point group C_{2h} has only four symmetry operations. There are 20 atoms in the orthorhombic unit cell (ferromagnetic *Pnma*) giving rise to 60 normal modes. The decomposition of the irreducible representation built on the basis of the Cartesian coordinates of the atoms in the unit cell leads to the following symmetry assignments for the 60 normal modes,

$$\Gamma_{\text{total}} = 18AU \oplus 18BU \oplus 12AG \oplus 12BG.$$

All 60 modes are active; of these 36 ($18AU \oplus 18BU$) modes are IR active and the remaining 24 modes ($12AG \oplus 12BG$) are Raman active. Among the 36 IR active modes three modes corresponds to translation ($1AU \oplus 2BU$). The calculated IR and Raman modes are presented in the Supplemental Material [46] and the corresponding simulated absorption spectra are plotted in Fig. 4. Intensities have been computed according to the CPHF/KS method [47–49].

A soft mode (with real frequency) at 84.6 cm^{-1} (BU) is observed with a very high IR intensity of about 1630 km mol^{-1}. A detailed analysis of this mode suggests that it corresponds to (O-Bi-O) rotation. If this mode had corresponded to a Bi-O displacement, it would have been responsible for an off-center driven ferroelectricity. Since the corresponding mode in the present calculation is rotational, the system stabilizes in the paraelectric phase rather than going for a phase transition to ferroelectric. Such a low-frequency part of the IR spectrum could be accurately verified by terahertz spectroscopy measurements.

The nature of each mode can be further analyzed by an isotopic substitution of the constituent atoms. Substitution of an isotope with higher mass compared to the original atom will result in a negative shift ($\Delta\nu$ cm^{-1}) in the modes (ν cm^{-1}). A shift less than $-5\,cm^{-1}$ can be ignored. In the present case the ^{209}Bi atom is substituted by a ^{212}Bi, ^{51}V is substituted by ^{54}V, and ^{16}O is substituted by ^{18}O. The shifts in the peak positions with respect to the isotopic substitution (one at a time) are shown in Fig. 5. As seen from the figure, the contribution of the vanadium atom is only to the IR active modes in the 200–400 cm^{-1} range, while the Bi atom contributes only to the modes in the low wave number range (60–110 cm^{-1}). The oxygen atoms contribute to all modes and the isotopic shift increases with the frequency. All Raman modes above

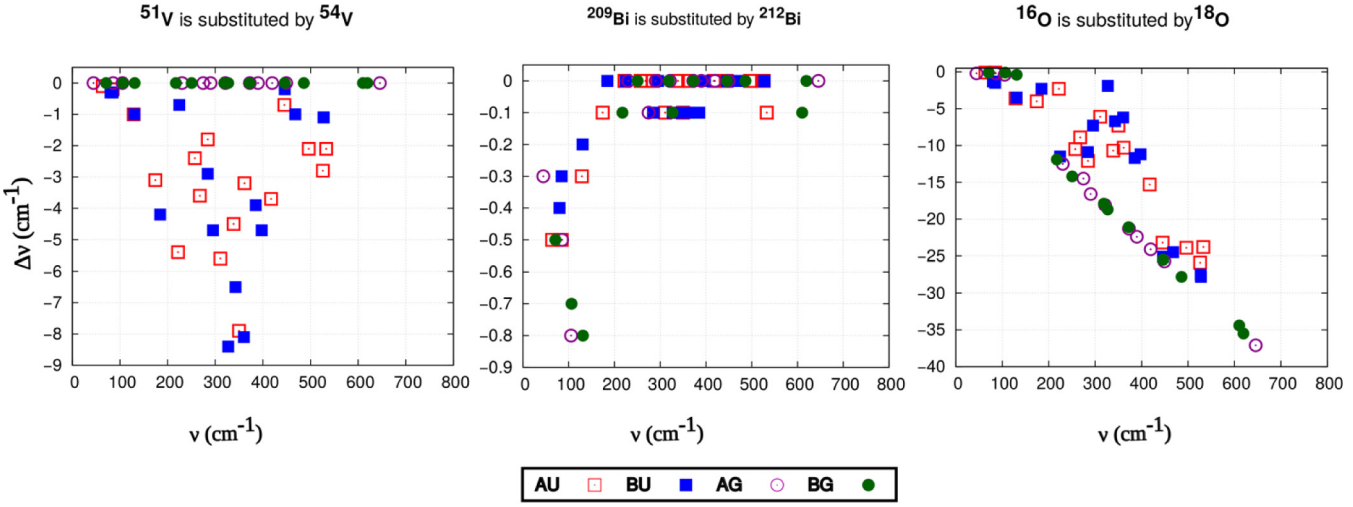

FIG. 5. The shifts in the infrared and Raman modes with respect to isotopic substitution are shown. ^{51}V is substituted by ^{54}V, ^{209}Bi is substituted by ^{212}Bi, and ^{16}O is substituted by ^{18}O.

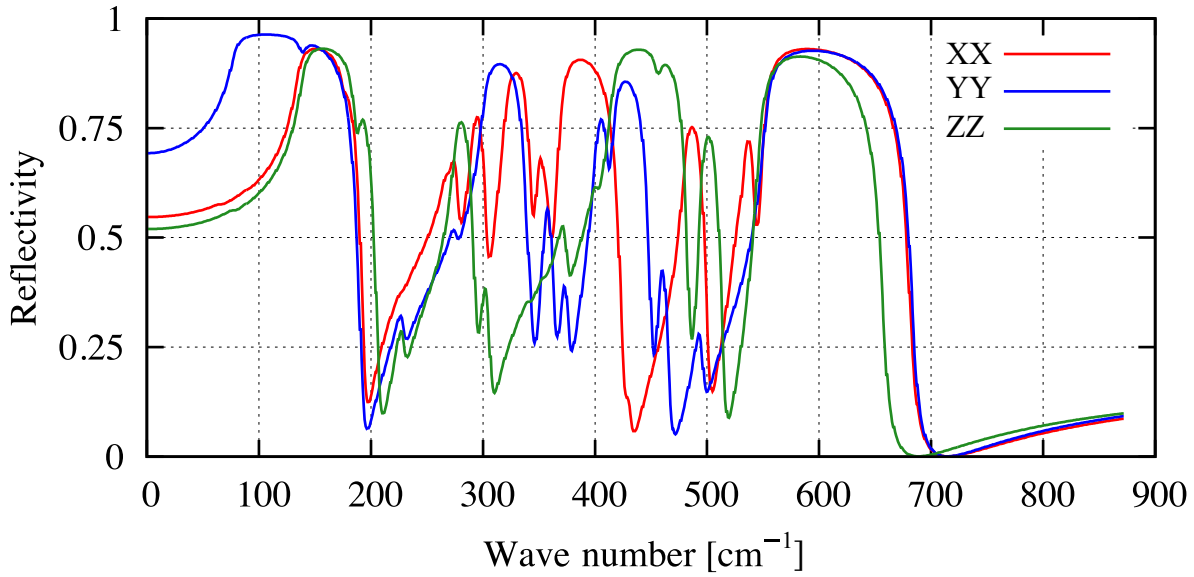

FIG. 6. Infrared reflectance spectrum of $BiVO_3$ calculated along three different axes, a, b, and c, as notated in the figure. The oscillator strengths are normalized to unity. The damping factor is set to 9 and the angle of incidence is kept as 10°.

100 cm^{-1} are affected by the isotopic substitution of oxygen. The shifts in the Raman modes are between 20 and 40 cm^{-1} in the high-frequency range.

The infrared reflectance curve $R_{ii}^{\text{fit}}(\nu)$ along the ii are calculated from modes and the oscillator strengths (ionic contribution to the static dielectric tensor) following the Fresnel formula [44,55] (see Supplemental Material for more details). The corresponding spectra for three different Cartesian directions are plotted in Fig. 6. Since no analogous experimental spectrum is available in the literature, we do not comment further on these spectra, but rather provide them as a reference for future experiments.

2. UV-VIS spectra

In Fig. 7, we plot the UV-vis absorption spectra of $BiVO_3$ calculated using the Coupled Perturbed Kohn-Sham (CPKS) method [50,56] as well as the sum over states (SOS) method for comparison. The SOS results were obtained from the zeroth iteration of CPKS, which does not include the orbital relaxation. In the low wavelength region both spectra give very similar results. On the other hand, in the higher wavelength region, the spectra are quite different. In the SOS state method, the first high intensity peak shows at 470 nm. However, due to orbital coupling in CPKS, the first adsorption peak is shifted to a higher wavelength of 550 nm. The calculated CPKS (CP-PBE0) spectrum indicates that an intense absorption peak appears at 2.25 eV (550 nm), right in the maximum of the sun light emission spectrum.

We have tested the stability of this result with respect to several computational parameters (such as density of reciprocal space sampling mesh, thresholds on exchange, and Coulomb integrals) and found its position reliable within an "error bar" of ±50 nm—in all cases, then, falling within the visible light range. The optical gap is found around 1.92 eV with a redshift of 0.1 eV with respect to the vertical gap as we have seen from the band structure. This is reasonable, as the vertical transition corresponding to 2.0 eV is of d-d type transition, which is only weakly allowed.

E. Magnetic properties

An analysis on the atomic integrated spin density of the $BiVO_3$ crystal at its ferromagnetic state is provided in Table V. The nominal spin density on the vanadium atoms, i.e., 1.980μ_B (V1) and 1.959μ_B (V2) are close to its ideal d^2 spin state (V^{3+}). The small difference in the atomic spin densities of V1 and V2 vanadium atoms are attributed to the slight difference in the strength of their covalent bonding with oxygen atoms. The atomic spin density map in the (110) and (010) planes are plotted in Fig. 8. As can be seen from the figure, most of

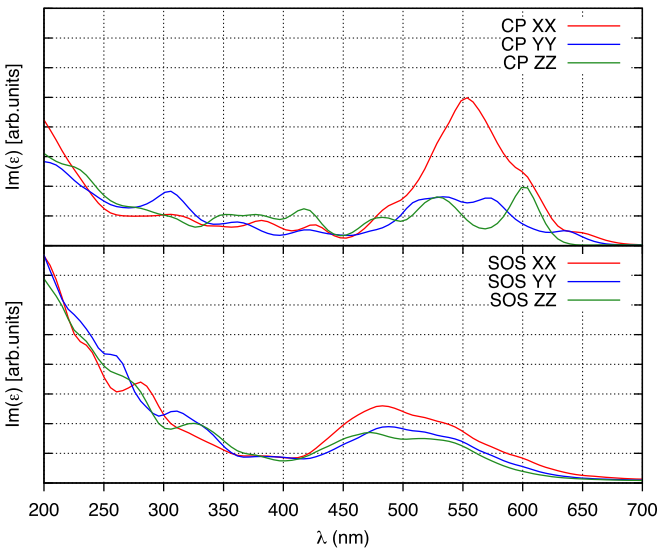

FIG. 7. UV-vis spectra of $BiVo_3$ calculated using either coupled-perturbed (CP, top panel) or sum over states (SOS, bottom panel) and a PBE16 hybrid functional.

TABLE V. Atomic spin density of all the irreducible atoms. The units are given in Bohr magnetons (μ_B).

Atom	Atomic spin (μ_B)
Bi	0.036
V1	1.980
V2	1.959
O1	−0.009
O2	0.013
O3	−0.010

the spin density is centered on the V sites. A non-negligible spin density is, however, visible both at the oxygen and the Bi sites. At the oxygen site, two variations of spin density can be seen. First, the negative spin corresponds to the delocalization of V-3*d* charge towards the oxygen sublattice due to the comparatively small V1-O1-V2 and V1-O3-V3 bond distance. Delocalization of charge towards the oxygen atoms induces an opposite polarization at the O1 and O3 oxygen sites, as a direct consequence of the hybridization between the vanadium and oxygen atoms (O1 and O3). This further substantiates the much higher Mulliken population density of V1-O1 (0.039 $|e|$), V2-O1 (0.038 $|e|$), V1-O3 (0.037 $|e|$), and V2-O3 (0.040 $|e|$) bond given in Table II. On the other hand, the spin density at the O2 oxygen is slightly positive ($+0.13\mu_B$). Due to the comparatively larger distance between the vanadium atoms (V1-O2-V2) in the *a*-*c* plane, the charge density around the oxygen atom accumulates close to the nucleus. As a consequence, a slightly higher positive spin density will result in the oxygen site. This can be seen from the spin density plot in the (010) plane given in Fig. 8. As a result of this, the hybridization between vanadium and O2 atoms is comparatively weaker. This weaker hybridization can be further inferred from the low bond population of 0.027 $|e|$ and 0.034 $|e|$ for the V1-O1 and V2-O2 bonds respectively (see Supplemental Material [46]). However, the spin density at the oxygen sites is smaller than the Bi site, indicating a weak superexchange interaction between the neighboring V atoms across oxygen. Strong superexchange interactions normally stabilize the AFM states and hence our finding on the relative stability of FM structure over the AFM structures is reinforced. The high value of spin density at the Bi site ($0.036\mu_B$) is attributed to the highly localized lone pair electrons giving rise to a strong negative bond population of Bi atoms (−0.069 $|e|$, −0.064 $|e|$and −0.089 $|e|$) with the oxygen atoms.

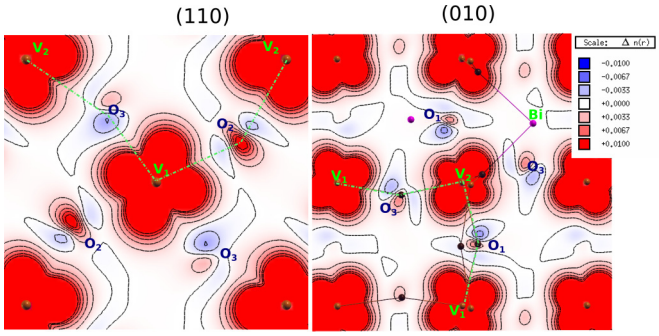

FIG. 8. Atomic spin-density map of ferromagnetic $BiVO_3$ in the (110) and (010) planes. Irreducible O, V, and Bi atoms are notated. Bondings in the considered plane are marked via dashed green lines. Nine contours are drawn from −0.01 to +0.01 $|e|$/bohr^3. Red portion represents portion with higher spin density.

F. Conclusions

Using density functional theory, a complete characterization of a ferromagnetic $BiVO_3$ perovskite in its othorhombic form is described. Although the electronic transition is found to be indirect in nature with a gap of 1.75 eV, a direct band gap of 1.96 eV is calculated at the Γ point. The calculated CPKS (CP-PBE0) UV-vis spectrum indicates that an intense absorption peak appears at 2.25 eV (550 nm), right in the maximum of the sunlight emission spectrum. Therefore the material is expected to be a good candidate for visible light driven photocatalytic applications. The valence and conduction bands show good dispersion, which is essential for enhancement in the charge transport properties. The exciton binding energy is calculated to be −7 meV which shows that the excitons can be easily dissociated at room temperature. The phonon frequencies at the center of the Brillouin zone are simulated. No unstable soft modes are identified and thus the dynamical stability of the material is confirmed. The simulated IR and Raman modes are provided and we believe that the simulated IR and Raman spectra could be a guideline for future experiments.

ACKNOWLEDGMENTS

The authors acknowledge financial support from the Slovenian Research Agency (Research Core Funding No. P2-0377). The authors also acknowledge "The Supercomputing Center of Galicia (CESGA)," HPC-Arctur Slovenia, Barcelona Super Computing Centre (BSC) Barcelona, Spain (under HPC-Europa 2) for providing supercomputing facilities.

[1] K. Maedal, K. Suzuki, Y. Yamashita, and Y. Mera, J. Phys.: Condens. Matter **12**, 10079 (2000).
[2] N. S. Lewis, Inorg. Chem. **44**, 6900 (2005).
[3] K. Hanjalic, R. van de Krol, and A. Lekić, *Sustainable Energy Technologies: Options and Prospects* (Springer-Verlag, New York, 2008).
[4] J. R. Bolton, S. J. Strickler, and J. S. Connolly, Nature (London) **316**, 495 (1985).
[5] N. Serpone, A. V. Emeline, V. K. Ryabchuk, V. N. Kuznetsov, Y. M. Artemńev, and S. Horikoshi, ACS Energy Lett. **1**, 931 (2016).
[6] L. Yuan, C. Han, M.-Q. Yang, and Y.-J. Xu, Int. Rev. Phys. Chem. **35**, 1 (2016).
[7] C. Acar, I. Dincer, and G. F. Naterer, Int. J. Energy Res. **40**, 1449 (2016).
[8] T. Jafari, E. Moharreri, A. S. Amin, R. Miao, W. Song, and S. L. Suib, Molecules **21**, 1 (2016).
[9] C. A. Grimes, O. K. Varghese, and S. Ranjan, *Light, Water, Hydrogen: The Solar Generation of Hydrogen by Water Photoelectrolysis* (Springer, New York, 2008).
[10] W. Liu, Y. H. Zhao, J. Nguyen, Y. Li, Q. Jiang, and E. J. Lavernia, Carbon **47**, 3452 (2009).

[11] J. R. Bolton, Solar Energy **57**, 37 (1996).
[12] A. J. Bard and M. A. Fox, Acc. Chem. Res. **28**, 141 (1995).
[13] M. D. Bhatt and J. S. Lee, J. Mater. Chem. A **3**, 10632 (2015).
[14] F. Fresno, R. Portela, S. Suarez, and J. M. Coronado, J. Mater. Chem. A **2**, 2863 (2014).
[15] K. Hashimoto, H. Irie, and A. Fujishima, Jpn. J. Appl. Phys. **44**, 8269 (2005).
[16] K. Sivula, F. Le Formal, and M. Grätzel, ChemSusChem **4**, 432 (2011).
[17] J. A. Seabold and K. S. Choi, J. Am. Chem. Soc. **134**, 2186 (2012).
[18] S. S. Kalanur, I.-H. Yoo, J. Park, and H. Seo, J. Mater. Chem. A **5**, 1455 (2017).
[19] A. Kudo and Y. Miseki, Chem. Soc. Rev. **38**, 253 (2009).
[20] A. Kudo, Pure Appl. Chem. **79**, 1917 (2007).
[21] K. Domen, S. Naito, M. Soma, T. Onishi, and K. Tamaru, J. Chem. Soc., Chem. Commun. **12**, 543 (1980).
[22] H. Kato and A. Kudo, J. Phys. Chem. B **105**, 4285 (2001).
[23] H. Kato, H. Kobayashi, and A. Kudo, J. Phys. Chem. B **106**, 12441 (2002).
[24] A. Kudo, K. Omori, and H. Kato, J. Am. Chem. Soc. **121**, 11459 (1999).
[25] C. Li, H. Wang, B. Wang, and R. Wang, Appl. Phys. Lett. **91**, 071902 (2007).
[26] C. Li, B. Wang, R. Wang, H. Wang, and X. Lu, Comput. Mater. Sci. **42**, 614 (2008).
[27] J. A. McLeod, Z. V. Pchelkina, L. D. Finkelstein, E. Z. Kurmaev, R. G. Wilks, A. Moewes, I. V. Solovyev, A. A. Belik, and E. Takayama-Muromachi, Phys. Rev. B **81**, 144103 (2010).
[28] J. H. Lee, X. Ke, R. Misra, J. F. Ihlefeld, X. S. Xu, Z. G. Mei, T. Heeg, M. Roeckerath, J. Schubert, Z. K. Liu, J. L. Musfeldt, P. Schiffer, and D. G. Schlom, Appl. Phys. Lett. **96**, 262905 (2010).
[29] K. Takahashi, N. Kida, and M. Tonouchi, Phys. Rev. Lett. **96**, 117402 (2006).
[30] P. Ravindran, R. Vidya, A. Kjekshus, H. Fjellvåg, and O. Eriksson, Phys. Rev. B **74**, 224412 (2006).
[31] X. Meng and Z. Zhang, J. Mol. Catal. A: Chem. **423**, 533 (2016).
[32] P. Baettig, C. Ederer, and N. A. Spaldin, Phys. Rev. B **72**, 214105 (2005).
[33] D. Khomskii, Physics **2**, 20 (2009).
[34] C. Ederer and N. A. Spaldin, Phys. Rev. Lett. **95**, 257601 (2005).
[35] D. I. Khomskii, J. Magn. Magn. Mater. **306**, 1 (2006).
[36] N. A. Hill, J. Phys. Chem. B **104**, 6694 (2000).
[37] L. Bi, A. R. Taussig, H.-S. Kim, L. Wang, G. F. Dionne, D. Bono, K. Persson, G. Ceder, and C. A. Ross, Phys. Rev. B **78**, 104106 (2008).
[38] A. A. Belik, J. Solid State Chem. **195**, 32 (2012).
[39] M. Dragomir and M. Valant, Ceram. Int. **39**, 5963 (2013).
[40] M. Goffinet, P. Hermet, D. I. Bilc, and P. Ghosez, Phys. Rev. B **79**, 014403 (2009).
[41] M. P. Singh and F. S. Razavi, AIP Conf. Proc. **1590**, 90 (2014).
[42] B. Liu, L.-J. Wu, Y.-Q. Zhao, L.-Z. Wang, and M.-Q. Cai, RSC Adv. **6**, 92473 (2016).
[43] M. W. Lufaso and P. M. Woodward, Acta Crystallogr. Sect. B **57**, 725 (2001).
[44] R. Dovesi, R. Orlando, C. M. Zicovich-Wilson, B. Civalleri, L. Maschio, A. Erba, S. Casassa, M. Ferrabone, M. D. L. Pierre, P. D'Arco, Y. Noël, M. Causà, M. Rérat, and B. Kirtman, Int. J. Quantum Chem. **114**, 1287 (2014).
[45] J. H. Skone, M. Govoni, and G. Galli, Phys. Rev. B. **89**, 195112 (2014).
[46] See Supplemental Material at http://link.aps.org/supplemental/10.1103/PhysRevB.96.165152 for the computational parameters used in the DFT calculations as well a detailed discussion about the structural parameters and electronic properties including the total, atom, and orbital projected density of states are given. In addition, the method for estimating the vibrational spectra using the Fresnel formula and the computed IR and Raman modes are provided.
[47] L. Maschio, B. Kirtman, R. Orlando, and M. Rérat, J. Chem. Phys. **137**, 204113 (2012).
[48] L. Maschio, B. Kirtman, M. Rérat, R. Orlando, and R. Dovesi, J. Chem. Phys. **139**, 164102 (2013).
[49] L. Maschio, B. Kirtman, M. Rérat, R. Orlando, and R. Dovesi, J. Chem. Phys. **139**, 164101 (2013).
[50] A. M. Ferrari, R. Orlando, and M. Rérat, J. Chem. Theory Comput. **11**, 3245 (2015).
[51] L. Vasylechko, A. Matkovskii, D. Savytskii, A. Suchocki, and F. Wallrafen, J. Alloys Compd. **291**, 57 (1999).
[52] H. G. Kim, D. W. Hwang, and J. S. Lee, J. Am. Chem. Soc. **126**, 8912 (2004).
[53] N. Ashcroft and N. Mermin, *Solid State Physics* (Saunders College, Fort Worth, 1976).
[54] T. Le Bahers, M. Rerat, and P. Sautet, J. Phys. Chem. C **118**, 5997 (2014).
[55] J. Decius and R. Hexter, in *Molecular Vibrations in Crystals* (McGraw-Hill, New York, 1977), p. 50.
[56] M. Ferrero, M. Rérat, B. Kirtman, and R. Dovesi, J. Chem. Phys. **129**, 244110 (2008).